Spinel-facies mantle xenoliths from Cerro Redondo, Argentine Patagonia: Petrographic, geochemical, and isotopic evidence of interaction between xenoliths and host basalt

M. Schilling[a,*], R.V. Conceição[b,c], G. Mallmann[b,d], E. Koester[b], K. Kawashita[b], F. Hervé[a], D. Morata[a], A. Motoki[e]

[a]*Facultad de Ciencias Físicas y Matemáticas, Departamento de Geología, Universidad de Chile, Plaza Ercilla 803, Santiago, Chile*
[b]*Laboratório de Geologia Isotópica, CPGq, IG, Universidade Federal do Rio Grande do Sul, Av. Bento Gonçalves, 9500, C.P. 15001, CEP 91501-970, Porto Alegre, RS, Brazil*
[c]*Departamento de Geologia, Universidade Federal do Rio Grande do Sul, CEP 91501-970 Porto Alegre, RS, Brazil*
[d]*Programa de Pós-graduação em Geociências, IG, Universidade Federal do Rio Grande do Sul, CEP 91501-970 Porto Alegre, RS, Brazil*
[e]*Departamento de Mineralogia e Petrologia Ignea, Faculdade de Geologia, Universidade do Estado do Rio de Janeiro, Rua Sao Francisco Xavier 524, Sala 4023, Bloco A, Maracana, Rio de Janeiro, RJ, Brazil*

Abstract

Cerro Redondo is an ancient cinder cone now almost completely eroded, sited over a sill that corresponds to a sub-volcanic magma chamber, in Santa Cruz province, Patagonia, Argentina. It is composed of Pliocene-Pleistocene alkaline basalt containing spinel-facies lherzolite and harzburgite mantle xenoliths. Core compositions of pyroxenes indicate temperatures of 823 °C to 1043 °C and pressures of 12.4 kb to 21.4 kb. Based on *P–T* estimates, petrographic, geochemical, and isotopic characteristics, we propose that Cerro Redondo xenoliths come from a thick homogeneous mantle column (36 km to 63 km depth), and present different degrees of basalt infiltration. A simple mixing model based on Sr isotopes was used to quantify the host basalt infiltration, and contamination values of 0.0%, 0.2%, 3%, and 12% were obtained for samples X-F, X-D, X-C, and X-B, respectively. For unknown reasons, samples X-G and X-E suffered selective isotopic and trace element modification, respectively, associated with ~1% of basalt infiltration. Sample X-F best represents the sub-continental lithospheric mantle column, conserving primary equilibrium textures with sharp grain boundaries, and having TiO_2, CaO, Na_2O, K_2O, and P_2O_5 contents lower than average spinel lherzolite, flat chondrite-normalized REE pattern, and $^{87}Sr/^{86}Sr$ and $^{143}Nd/^{144}Nd$ ratios of 0.70519 and 0.51297, respectively. This sample records a decoupling of the Sr–Nd system where Sr ratios increase at constant Nd ratios, possibly caused by chromatographic processes. Its $^{206}Pb/^{204}Pb$, $^{207}Pb/^{204}Pb$, and $^{208}Pb/^{204}Pb$ ratios are 17.987, 15.556, and 37.959, respectively. As the

* Corresponding author. Tel.: +56 2 6784108; fax: +56 2 6963050.
E-mail address: mschilli@cec.uchile.cl (M. Schilling).

interaction with the host basalt increases, xenoliths show a gradual increase of disequilibrium textures such as reaction rims and exsolution lamellae in orthopyroxene and clinopyroxene, and increase of TiO_2, CaO, Al_2O_3, Na_2O, K_2O, P_2O_5, LREE, and incompatible element concentrations. The Sr–Nd system shows an unusual positive trend from the unmodified sample X-F toward the host basalt isotope composition with $^{87}Sr/^{86}Sr$ and $^{143}Nd/^{144}Nd$ ratios of 0.70447 and 0.51279, respectively, while $^{206}Pb/^{204}Pb$, $^{207}Pb/^{204}Pb$, and $^{208}Pb/^{204}Pb$ ratios tend to increase toward those of the host basalt (18.424, 15.648, and 38.728, respectively) as the xenolith–basalt interaction increases. The basalt–xenolith reaction probably started during the transport of the xenoliths to the surface, and continued during the residence of xenoliths in the sub-volcanic magma chamber of Cerro Redondo.

Keywords: Santa Cruz Province—Argentina; Alkaline basalt; Sub-continental lithospheric mantle; Spinel lherzolite–harzburgite; Basalt infiltration

1. Introduction

Ultramafic mantle xenoliths are found in the Pliocene–Recent alkaline basalt province, east of the Andes from 40°S to 52°S. They are mainly spinel-facies peridotites (Ramos et al., 1982; Gorring and Kay, 2000; Laurora et al., 2001; Ciuffi et al., 2002), and exceptionally garnet-facies peridotites (Stern et al., 1999; Kempton et al., 1999a,b; Kilian and Stern, 2002). These types of xenoliths have been the focus of many studies during recent years as they record chemical and compositional variability, and the effects of different processes in the lithospheric mantle. Previous studies have shown that the Patagonian mantle lithosphere represented by xenoliths underwent various processes, such as variable degrees of melt extraction, carbonatitic metasomatism ascribed either to the asthenosphere (Gorring and Kay, 2000) or to the subducted slab (Laurora et al., 2001), adakitic metasomatism (Kilian and Stern, 2002), and basalt infiltration (Ciuffi et al., 2002).

Cerro Redondo is a volcanic body formed of Pliocene–Pleistocene alkaline basalt, bearing many spinel-facies mantle xenoliths. In this paper we report petrography, mineral and whole-rock chemistry, and Sr–Nd–Pb isotopic data for the host basalt and six samples of xenoliths. We will demonstrate that the dominant process controlling the composition of Cerro Redondo xenoliths is basalt infiltration/chemical interaction, which produces chemical characteristics commonly found in metasomatized mantle xenoliths. In addition, we try to constrain the composition of the lithospheric mantle under Cerro Redondo area as recorded by unmodified xenoliths.

2. Geological setting

Cerro Redondo is located approximately 60 km south of Gobernador Gregores, Santa Cruz province, Argentina (Fig. 1), in the southwestern corner of the Deseado Massif. It lies within the basaltic plateau known as Meseta Central, ~250 km east of the volcanic gap between the Southern Volcanic Zone (SVZ) and the Austral Volcanic Zone (AVZ), which is attributed to subduction of the Chile ridge (Cande and Leslie, 1986).

Cerro Redondo has a dome form, with a semi-circular base of ~800 m in diameter and a height of ~300 m above alluvial deposits of the Río Chico. The upper part of the volcanic edifice is formed by beds of welded scoria, 50 to 100 m thick, while the lower part is a massive body with well-developed sub-vertical columnar jointing. The contact between these units is irregular. This structure is interpreted as an ancient cinder cone, now almost completely eroded, located over a sill that corresponds to a sub-volcanic magma chamber. Some pyroclastic bombs can be found on the slopes of Cerro Redondo.

The ultramafic xenoliths are fresh and dispersed in the basalt. They have sub-spherical or ellipsoidal forms, with long axis ranging from 2 to 30 cm. They are usually well rounded, although there are samples with polygonal and faceted shapes, and they comprise ~5% to 10% of the total volume of the rock. The basalt–xenolith contacts are sharp and, macroscopically, no reaction rims between the basalt and the xenoliths were

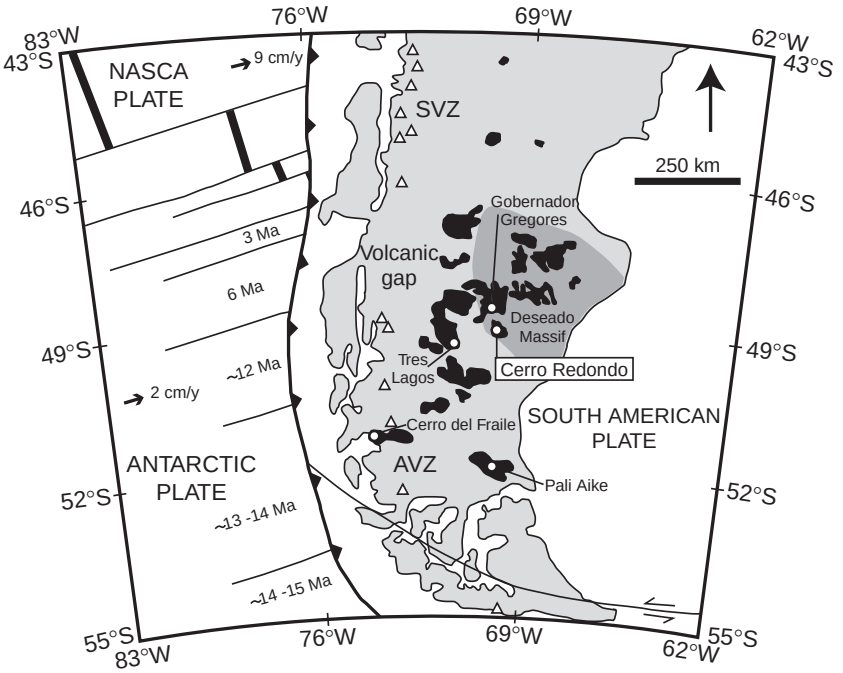

Fig. 1. Location map of Cerro Redondo and other mantle xenolith occurrences in southern Patagonia (modified from Gorring and Kay, 2000). The tectonic setting, distribution of the Neogene plateau lavas (in black), and the volcanic centers (△) of the Southern and Austral Volcanic Zones (SVZ and AVZ, respectively) are also shown. Timings of ridge collisions between fracture zones on the Antarctic Plate (Cande and Leslie, 1986; Gorring et al., 1997) are shown.

observed. The xenoliths rarely have a reddish color, probably caused by the alteration of olivine crystals to iddingsite.

3. Analytical techniques

The petrography and texture of the xenoliths were examined by optical microscope. Modal composition of xenoliths was calculated by counting over 2000 points. The host basalt and six samples of xenoliths with diameter grater than 5 cm were crushed in agate mortar. For the major and trace element measurement, 0.5 g and 5 g, respectively of each sample powder, were treated with HF and $HClO_4$, then leached with HCl. REE were co-precipitated with iron in ammonium hydroxide, and then loaded in an acid medium on ion exchange columns (5OWX8-Dowex); element concentrations were measured by ICP-AES. The international standard for calibration was DNC-1. The major element compositions of minerals of the host basalt and 5 xenoliths were determined by electron microprobe at the University Pierre et Marie Curie, Paris, on a Camebax SX-50, using an accelerating voltage of 15 kV, a beam current of 40 nA, and a count time of 20 s. Sample X-G was analyzed by microprobe at the Universidad de Chile on a SEM-probe Camebax SU-30 using an accelerating voltage of 15 kV, a beam current of 10 nA, and a count time of 10 s.

Samples for radiogenic isotope analysis were spiked with mixed ^{87}Rb–^{84}Sr and ^{149}Sm–^{150}Nd tracer and processed using standard dissolution procedures with HF, HNO_3 and HCl in Teflon vials, warmed on a hot plate until complete material dissolution. Cationic AG-50W-X8 (200–400 mesh) resin columns were used in order to separate the Rb, Sr, and REE, followed by Sm and Nd separation using anionic LN-B50-A (100–200 μm) resin. Pb was separated using anionic A8-B500-F-CL (200–400 mesh) resin in HBr solution. Each sample was completely dried and then loaded with 0.25 N H_3PO_4 (Rb, Sr, Sm, and Nd), plus silica gel (Pb), onto appropriate filaments (single

Ta for Rb, Sr, Sm, Pb, and triple Ta–Re–Ta for Nd). The samples were run in a multi-collector VG Sector 54 thermal ionization mass spectrometer at Laboratório de Geologia Isotópica (Universidade Federal do Rio Grande do Sul, Brazil) in the static mode. Sr and Nd ratios were normalized to $^{86}Sr/^{88}Sr=0.1194$ and $^{146}Nd/^{144}Nd=0.7219$, respectively. Measurements for the NIST standard NBS-987 gave $^{87}Sr/^{86}Sr=0.710260\pm0.000014$, and for La Jolla gave $^{143}Nd/^{144}Nd=0.511859\pm0.000010$. For Pb NBS-981 and NBS-982, variation from accepted values was less than 0.01%/a.m.u. Total blanks averaged <150 pg for Sr and Sm, <750 pg for Nd, and <200 pg for Pb.

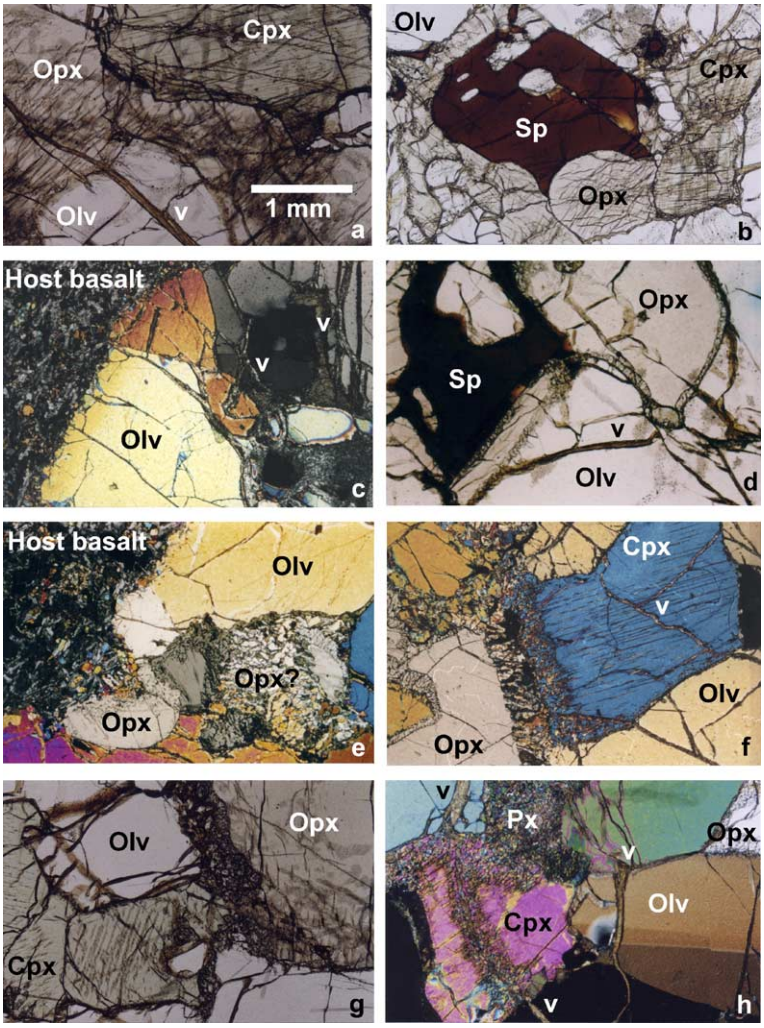

Fig. 2. Photomicrographs of thin sections showing textural variations of the Cerro Redondo xenoliths. Scale is the same in all photographs. Panels c, e, f, h With crossed polarizers, and all others with plane polarized light. (a) Sharp crystal boundaries reflecting equilibrium textures in the mineral assemblage of sample X-D. Some brownish veinlets (v) are observed cutting grain boundaries. (b) Sample X-F with similar textures to sample X-D (a) showing vermicular spinel with and olivine inclusions. (c) Xenolith (X-G)–basalt contact showing color change of olivine towards the host basalt probably due to diffusion process. In addition, veinlets cutting a crystal of olivine, preferentially oriented normal to the xenolith–basalt contact are observed. (d) Sample X-G where thin reaction rims in orthopyroxene and spinel, and thin brownish veinlets are observed. (e) Dissolution and recrystallization of pyroxene into fine-grained (Opx?) aggregates in sample X-E. (f–g) Sample X-B showing thick reaction rims in Opx and Cpx, and exsolution lamellae mainly in Cpx. (h) Recrystallized pyroxene with mosaic texture associated to brownish veins in sample X-C. (For interpretation of the references to colour in this figure legend, the reader is referred to the web version of this article.)

4. Petrography and mineralogy

4.1. Host basalt

The host rock is a fresh porphyritic basalt with olivine xenocrysts, up to 3 mm in size, which have a high forsterite content ($Fo_{90–91}$), and exhibit kink bands. There are also some pyroxene xenocrysts (~2 mm in size), almost completely recrystallized into very fine-grained mosaics, which makes distinction between clinopyroxene and orthopyroxene difficult. The groundmass has an intergranular texture (Fig. 2c, e) formed by 0.1 to 0.3 mm long microlites of sanidine (An_5, Ab_{45}, Or_{50}), andesine (An_{44}, Ab_{54}, Or_2), olivine ($Fo_{65–79}$), and clinopyroxene (En_{43}, W_{45}, Fs_{12}), together with opaque minerals, small apatite crystals (<0.1 mm), and glass. Nepheline aggregates are mainly seen at some xenolith–basalt contacts and around some recrystallized pyroxene xenocrysts, and also occur dispersed in the basalt.

4.2. Xenoliths

The main petrographic and mineralogical features of the studied xenoliths are presented in Table 1, and microphotographs are shown in Fig. 2. Detailed descriptions can be found in Schilling (2002). The mineral composition of some representative crystals is shown in Table 2.

According to their modal compositions, five of the six studied ultramafic xenoliths are anhydrous spinel lherzolites, while one sample (X-F) corresponds to an anhydrous harzburgite. Following the classification of Mercier and Nicolas (1975) all these xenoliths have a protogranular texture, defined by coarse-grained olivine and orthopyroxene (5 and 9 mm, respectively), blebs of clinopyroxene, and much finer-grained vermicular spinel (1 mm). Some pyroxene crystals show deformation textures. Many olivine and pyroxene crystals have fluid inclusions, commonly disposed in linear arrays, interpreted as secondary inclusions. Under the microscope, some olivine crystals in contact with the host basalt show zoned rims probably due to diffusion processes (Fig. 2c), while some pyroxene crystals are recrystallized into fine-grained mosaic aggregates (Fig. 2e).

Based on their petrography, this xenolith suite presents a gradational variation defined mainly by the increasing development of disequilibrium textures. We will use this variation to order the samples in Fig. 2 and in all data tables, and will show that there is also a concordant gradation of the whole rock chemistry and isotopic ratios, discussed in the next sections:

(1) Samples X-D (Fig. 2a, b) and X-F (Fig. 2c) show equilibrium textures defined by sharp grain boundaries. Only subtle exsolution lamellae and thin reaction rims are observed in

Table 1
Summary of petrography and mineralogy, and pressure–temperature estimates for Cerro Redondo xenoliths

Sample	X-F	X-D	X-G	X-E	X-E	X-B	X-C	X-C
	Sp.H	Sp.Lh	Sp.Lh	Sp.Lh		Sp.Lh	Sp.Lh	
Texture	Prot. I	Prot. I	Prot. I	Prot. I	rims	Prot. I	Prot. I	rims
Modal composition (%)								
Olv	57.1	71.6	60.6	72.8		70.1	62.0	
Opx	38.4	15.7	27.8	12.6		19.7	23.8	
Cpx	3.0	11.4	10.9	11.8		8.4	11.3	
Sp	1.5	1.3	0.7	2.9		1.8	2.9	
Equilibration pressures (kb)								
M	35.9	21.4	20.9	12.4		15.9	16.3	
Equilibration temperatures (°C)								
W-B	1064	1059	1095	988	1007	974	1004	1085
B-M	1138	1138	1253	1074	1001	868	962	1180
B-K	1023–1042	992–1010	841–853	823–836	994–1013	913–930	920–935	995–1014

Sp.H: spinel harzburgite; Sp.Lh: spinel lherzolite; Prot. I: protogranular type I; rims: temperatures estimates using rim compositions; Olv: olivine; Opx: orthopyroxene; Cpx: clinopyroxene; Sp: spinel; M: Geobarometer of Mercier et al., 1984; Geothermometers of W-B: Wood and Banno (1973); B-M: Bertrand and Mercier (1985); B-K: Brey and Köhler (1990).

Table 2
Major element compositions of core and rim of minerals from the Cerro Redondo xenoliths

Sample	X-F								X-D						X-E						
Phase	Ol (77)	Opx (73)	Opx (76)	Cpx (74) core	Cpx (75) rim	Sp (70)	vein	vein	Ol (22)	Ol (25)	Opx (21)	Opx (26)	Cpx (27)	Sp (20)	Ol (40)	Ol (44)	Opx (41) core	Opx (42) rim	Cpx (47) core	Cpx (48) rim	Sp (39)
SiO_2	41.61	56.82	57.05	53.40	50.78	0.15	43.14	44.02	40.78	40.94	55.78	56.52	52.18	0.08	41.17	41.11	57.02	59.91	51.11	54.60	0.03
TiO_2	0.03	0.09	0.11	0.39	0.49	0.19	0.00	0.18	0.00	0.00	0.05	0.09	0.36	0.15	0.01	0.00	0.11	0.16	0.52	0.44	0.15
Al_2O_3	0.07	3.32	3.85	6.48	4.83	49.14	2.2	0.7	0.01	0.01	3.59	3.40	5.82	50.28	0.02	0.00	3.80	0.72	5.73	4.78	49.34
Cr_2O_3	0.00	0.43	0.59	1.72	1.35	17.48	0.00	0.00	0.03	0.00	0.38	0.38	1.30	16.64	0.15	0.02	0.57	0.20	1.27	0.86	18.39
FeO	8.26	5.87	5.85	2.24	2.71	11.14	4.91	4.56	8.85	8.58	5.71	5.34	2.11	10.71	9.27	8.70	5.60	5.76	1.77	2.22	11.12
MnO	0.20	0.11	0.05	0.16	0.03	0.13	0.02	0.08	0.16	0.26	0.05	0.09	0.10	0.09	0.18	0.18	0.21	0.07	0.04	0.03	0.13
MgO	49.81	34.17	33.74	14.95	16.75	20.37	35.17	34.82	49.16	49.20	33.60	33.28	15.19	19.47	48.49	49.40	32.99	34.07	14.90	15.30	19.39
CaO	0.10	0.49	0.61	19.98	20.45	0.01	0.09	0.2	0.09	0.18	0.57	0.51	20.13	0.06	0.12	0.02	0.53	1.07	21.14	21.17	0.06
Na_2O	0.00	0.08	0.06	1.87	0.63	0.01	0.00	0.03	0.01	0.01	0.11	0.10	1.57	0.01	0.00	0.00	0.04	0.01	1.53	1.20	0.00
K_2O	0.00	0.00	0.00	0.00	0.00	0.00	0.08	0.06	0.01	0.03	0.00	0.00	0.00	0.00	0.00	0.01	0.00	0.00	0.00	0.00	0.00
NiO	0.31	0.16	0.09	0.00	0.10	0.43	0.08	0.00	0.35	0.31	0.14	0.09	0.05	0.37	0.35	0.30	0.02	0.08	0.00	0.03	0.39
Total	100.39	100.53	101.98	101.20	98.11	99.04			99.44	99.51	99.97	99.81	98.80	97.85	99.77	99.73	100.90	102.07	97.99	100.63	99.03
Mg#	0.91	0.93	0.91	0.92	0.94	0.82			0.91	0.91	0.92	0.92	0.93	0.80	0.90	0.91	0.91	0.91	0.97	0.93	0.79
Cr#						0.19								0.18							0.20
Fo	0.91								0.91	0.91					0.90	0.91					
En		90.20	90.01	48.80	50.08						90.20	90.70	49.20				90.10	89.40	47.90	48.10	
Fs		8.90	8.82	4.40	4.70						8.70	8.30	4.00				8.90	8.60	3.30	4.00	
Wo		0.90	1.17	46.80	44.60						1.10	1.00	46.80				1.00	2.00	48.80	47.90	

Sample	X-G						X-B		X-B									X-C						
Phase	Ol (17′)	Opx (1′)	Opx (16′)	Cpx (14′)	Cpx (4′)	Sp (6′)	Ol (6)	Ol (2)	Opx (5)	Opx (4)	Opx (16)	Opx (15)	Cpx (17)	Sp (13)	vein	vein	vein	Ol (38)	Opx (33)	Opx (32)	Cpx (29)	Cpx (28)	Cpx (31)	Sp (34)
									core	rim	core	rim							core	rim		core	rim	
SiO_2	40.49	55.89	54.67	51.90	52.06	0.02	41.40	41.53	54.84	55.79	54.51	57.07	52.20	0.00	46.90	47.89	1.52	40.14	54.73	56.29	52.43	51.73	52.23	0.02
TiO_2	0.05	0.13	0.08	0.48	0.45	0.07	0.00	0.00	0.10	0.10	0.09	0.15	0.49	0.06	0.02	0.00	0.08	0.00	0.17	0.12	0.56	0.45	0.49	0.10
Al_2O_3	0.00	4.44	4.14	5.83	6.24	51.21	0.00	0.00	4.06	3.57	4.32	0.96	5.96	48.91	3.49	3.74	0.14	0.01	4.21	1.26	5.58	6.12	2.58	48.41
Cr_2O_3	0.05	0.65	0.41	1.37	0.91	19.39	0.08	0.02	0.50	0.53	0.59	0.55	1.21	18.38	0.02	0.00	0.00	0.07	0.54	0.58	1.33	1.37	1.17	18.14
FeO	9.07	5.64	5.56	2.05	1.93	11.07	8.57	8.79	5.54	5.40	5.87	5.61	2.20	10.96	7.50	1.79	0.31	8.52	5.78	6.34	2.06	1.95	2.65	11.24
MnO	0.18	0.10	0.17	0.14	0.13	0.27	0.11	0.07	0.11	0.00	0.13	0.11	0.17	0.25	0.09	0.07	0.03	0.24	0.12	0.20	0.09	0.08	0.18	0.11
MgO	52.50	36.12	35.66	15.77	16.25	20.60	48.84	49.01	33.17	32.85	32.85	33.59	14.16	19.17	28.08	32.92	0.77	49.69	33.24	32.24	14.73	14.46	16.88	19.55
CaO	0.19	0.41	0.28	22.19	21.65	20.60	0.16	0.11	0.65	0.94	0.35	1.26	20.64	0.03	1.00	0.56	62.4	0.12	0.67	1.46	20.77	21.08	21.51	0.06
Na_2O	0.00	0.01	0.07	1.46	1.52	0.01	0.02	0.00	0.05	0.05	0.05	0.08	1.58	0.04	0.04	0.04	0.01	0.00	0.05	0.11	1.59	1.69	0.51	0.03
K_2O	0.00	0.00	0.00	0.00	0.00	0.00	0.01	0.00	0.00	0.00	0.00	0.00	0.00	0.00	0.10	0.14	0.00	0.00	0.00	0.00	0.00	0.00	0.00	0.00
NiO	0.63	0.00	0.06	0.02	0.08	0.39	0.26	0.28	0.06	0.12	0.18	0.00	0.00	0.34	0.23	0.01	0.04	0.32	0.03	0.00	0.15	0.04	0.01	0.21
Total	103.15	103.40	101.11	101.20	101.23	103.03	99.45	99.81	99.10	99.39	98.94	99.38	98.61	98.14	87.47	87.16	65.30	99.11	99.54	98.75	98.28	98.96	98.23	97.89
Mg#	0.91	0.97	0.98	0.97	0.94	0.80	0.91	0.91	0.92	0.92	0.91	0.91	0.92	0.79				0.91	0.92	0.91	0.93	0.94	0.92	0.80
Cr#						0.20								0.21										0.20
Fo	0.90						0.91	0.91										0.91						
En		91.07	91.20	47.86	49.30				90.10	89.90	90.10	89.10	46.70						89.70	87.20	47.7	47.00	49.80	
Fs		8.19	8.30	3.76	3.50				8.60	8.20	9.20	8.50	4.40						9.00	9.90	3.9	3.70	4.70	
Wo		0.74	0.50	48.38	47.20				1.30	1.90	0.70	2.40	48.90						1.30	2.90	48.4	49.30	45.60	

The analyses not specified correspond to core compositions. In parenthesis is the label number of each analysis. Veins analyses are also shown. Mg#=Mg/(Mg+Fe^{2+}); Cr#=Cr/(Cr+Al); Fo: fosterite; En: enstatite; Fs: Ferrosilite; Wo: wollastonite.

clinopyroxenes. Sample X-D shows incipient foliation marked by the orientation of fractures in olivine crystals.

(2) Samples X-G (Fig. 2d) and X-E (Fig. 2e) are characterized by incipient development of disequilibrium textures such as thin reaction rims on spinel, clinopyroxene and especially on orthopyroxene (Fig. 2d), and thin exsolution lamellae in both pyroxenes.

(3) Finally, samples X-B (Fig. 2f, g) and X-C (Fig. 2h) have strongly developed reaction textures such as exsolution lamellae and reaction rims on clinopyroxene and especially on orthopyroxene (Fig. 2f, g). Some pyroxenes are strongly recrystallized into fine-grained aggregates with mosaic shapes around veins (Fig. 2h) and next to the xenolith–basalt contact.

In spite of textural differences, the major element chemistry of mineral cores of all these xenoliths is quite constant (Table 2): olivine compositions are $Fo_{90–91}$, and clinopyroxene compositions are $En_{47–49}$, $Wo_{47–49}$, $Fs_{3–4}$ Cr-diopside, with 0.91–1.72 wt.% Cr_2O_3, 1.46–1.87 wt.% Na_2O, and 5.73–6.48 wt.% Al_2O_3. Clinopyroxene rims are poorer in Al, Cr, and Na, and richer in Fe, Mg, and Ca compared to the cores. The orthopyroxene cores are enstatites $En_{90–91}$, $Wo_{0.5–1.3}$, $Fs_{8.3–9.2}$, and progressive enrichment of Ca and impoverishment of Al is observed from core to rim. The Cr# (Cr#=Cr/(Cr+Al) as molecular ratio) in spinel crystals ranges from 0.18 to 0.21.

Brownish veinlets cut across fractures into the minerals of all xenolith samples. Their petrography suggests that they were probably formed under brittle conditions (Fig. 2a, c, d, f, and h). Their compositions obtained with microprobe analysis are quite imprecise and the sum of analyzed elements does not reach more than 88% (Table 2), indicating that some elements present were not analyzed, or that a large quantity of volatile elements is present. They have SiO_2 contents (43–48%) similar to olivine crystals but lower MgO concentrations (28–35%). The veinlets from X-B have relatively high contents of CaO, especially analysis (12) in Table 2, with a composition similar to carbonates with 62% of CaO and very low SiO_2 and MgO contents (1.5 and 0.8, respectively).

5. *P–T* estimates

In order to estimate the equilibrium conditions of Cerro Redondo xenoliths we use the mineral core compositions because they are least variable, while rim compositions are clearly associated to disequilibrium processes. The geobarometer of Köhler and Brey (1990), which is commonly used for spinel lherzolites, yielded unreasonable pressures. The empirical geobarometer based on Ca exchange between orthopyroxene and clinopyroxene of Mercier et al. (1984) yields meaningful pressure estimates in the spinel stability field (10 kb–20 kb), except for sample X-F (Table 1). Sample X-D and X-G yielded higher pressures (21.4 kb and 20.9 kb, respectively) close to the spinel-garnet transition. Samples X-B and X-C yielded intermediate pressures (15.9 kb and 16.3 kb, respectively) and sample X-E yielded the lowest pressure (12.4 kb).

The crystallization temperatures (Table 1) were estimated using various two-pyroxene geothermometers (Wood and Banno, 1973, (W-B); Bertrand and Mercier, 1985, (B-M); Brey and Köhler, 1990, (B-K)). The mathematical equations were resolved

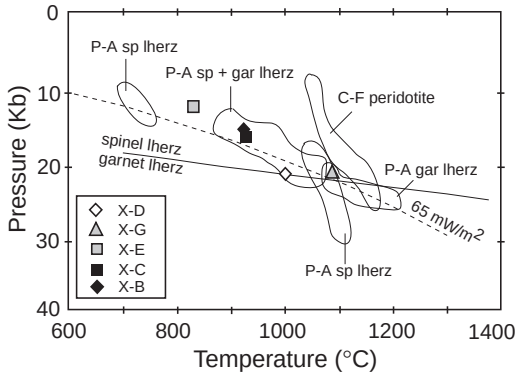

Fig. 3. Estimates of temperature (based on the geothermometer of Brey and Köhler, 1990) and pressures (based on the empirical geobarometer of Mercier et al., 1984) of equilibration applied to mineral core compositions of the Cerro Redondo xenoliths. Temperature for sample X-G was estimated using the geothermometer of Wood and Banno (1973). Spinel–garnet transition boundaries from O'Neill (1981). The *P–T* conditions of Pali-Aike (Kempton et al., 1999a) and Cerro del Fraile (Kilian and Stern, 2002) xenoliths are shown for comparison. Stern et al. (1999) calculate a geotherm close to the 65 mW/m of Chapman (1986) for Pali-Aike xenoliths. The *T* and *P* estimates for Cerro Redondo xenoliths plot close to the previous estimated Pali-Aike geotherm.

using the programme PTMAFIC (Soto and Soto, 1995). Temperature estimates using (B-K) require an estimate of pressure, so two solutions have been calculated based on 10 kb and 20 kb, and appear as a range in Table 1. In general, the different geothermometers are consistent with each other, but temperature ranges are different. The geothermometer that best complies with the estimated pressures is B-K, so we consider these temperatures as the best approximation to the equilibrium temperatures of Cerro Redondo xenoliths. The only exception is sample X-G that yielded an underestimated temperature of B-K (845 °C) for an estimated pressure of 20.9 kb. On the other hand, B-M yields an overestimate of 1253 °C. We think that the best temperature estimate for this sample is given by W-B (1095 °C). Samples X-F and X-D have the highest estimated temperatures (~1030 °C and 1000 °C, respectively), samples X-B and X-C have equilibration temperatures from 920 °C to 925 °C, and sample X-E yielded the lowest equilibration temperature of ~830 °C.

Table 3
Major (wt.%) and trace element (ppm) concentrations for Cerro Redondo xenoliths and host lava

Sample	X-F	X-D	X-G	X-E	X-B	X-C	McD	H-B
SiO_2	44.15	43.03	44.25	43.98	43.17	42.32	44.00	48.58
TiO_2	0.06	0.05	0.09	0.09	0.35	0.13	0.09	2.55
Al_2O_3	1.94	2.07	1.90	1.69	3.47	2.26	2.27	14.71
Fe_2O_3	1.70	1.45	1.18	3.72	1.89	1.69	0.00	3.13
FeO	5.84	6.54	6.38	4.62	6.91	6.73	8.43	6.54
MnO	0.11	0.12	0.12	0.10	0.13	0.12	0.14	0.13
MgO	42.39	43.00	42.40	42.00	38.60	42.40	41.40	7.56
CaO	0.97	1.16	1.28	1.44	2.16	1.78	2.15	6.06
Na_2O	0.20	0.18	0.23	0.26	0.71	0.35	0.24	4.30
K_2O	0.02	0.01	0.01	0.05	0.36	0.06	0.05	2.60
P_2O_5	0.04	0.03	0.03	0.05	0.13	0.05	0.06	0.82
LOI	1.58	1.71	1.36	1.13	1.52	1.45	-	2.78
Sum	99.00	99.34	99.23	99.13	99.40	99.37	98.80	99.76
Mg#	0.91	0.91	0.91	0.90	0.89	0.90	0.89	0.59
Trace elements								
La	0.26	0.35	0.25	0.65	5.00	1.70	2.60	46.00
Ce	0.60	0.90	0.60	1.40	13.10	3.90	6.29	108.00
Nd	0.45	0.55	0.46	0.85	6.95	2.40	2.67	54.00
Sm	0.12	0.13	0.15	0.21	1.28	0.33	0.47	9.87
Eu	0.04	0.06	0.06	0.08	0.36	0.15	0.16	2.75
Gd	0.15	0.15	0.20	0.26	1.00	0.43	0.60	7.28
Dy	0.20	0.19	0.24	0.26	0.78	0.39	0.51	4.27
Ho	0.04	0.04	0.05	0.05	0.13	0.07	0.12	0.70
Er	0.14	0.12	0.15	0.15	0.21	0.18	0.30	1.43
Yb	0.15	0.12	0.15	0.16	0.21	0.17	0.26	1.38
Lu	0.02	0.02	0.03	0.02	0.03	0.02	0.04	0.23
Y	1.1	1.1	1.2	1.3	3.7	1.9	4.4	19
Sc	8	9	9	8	10	10	12.2	13
Zn	44	49	50	43	62	45	65	123
Co	68	74	72	68	74	78	112	45
Ni	2443	2014	2420	2270	1610	2030	2160	178
Ba	13	11	12	15	88	36	33	556
Cr	2210	2700	2240	1700	2100	2010	2690	250
V	38	38	45	38	51	44	56	137
Cu	11	30	13	20	19	22	11	26
Sr	9	8	9	18	125	43	49	880
Zr	3.5	6	3.7	6.5	46	18	21	230

Mg#=Mg/(Mg+Fe) as molecular ratio.

Rim compositions for samples X-E and X-C (the only samples where we have analyzed both pyroxene rims) yield higher temperatures than cores (Table 1). This is probably a consequence of a last thermal event related to the heating of xenoliths during transport and interaction with the host magma, which would be responsible for the disequilibrium textures. A similar heating event is recorded in high-temperature garnet peridotites from Pali-Aike (Stern et al., 1999).

In Fig. 3 we show a *P–T* diagram for Cerro Redondo xenoliths where the fields of Cerro del Fraile peridotites (Kilian and Stern, 2002) and Pali-Aike xenoliths (Kempton et al., 1999a,b) are also shown. The *P–T* estimates for Pali-Aike xenoliths of Stern et al. (1999) plot close to the 65 mW/m^2 geotherm of Chapman (1986). Cerro Redondo xenoliths show similar *P–T* conditions to previously published results for Pali-Aike but restricted to the spinel stability field and can be interpreted as defining a Pliocene–Pleistocene paleogeotherm with characteristics similar to the Late Tertiary–Quaternary palegeotherm inferred for southern South America (Kempton et al., 1999a,b, Stern et al., 1999).

6. Bulk-rock major and trace element composition

The results of the bulk rock chemical analysis of Cerro Redondo xenoliths and host basalt are presented in Table 3, where the average for spinel lherzolites of alkaline continental basalts compiled by McDonough (1990) is given for comparison.

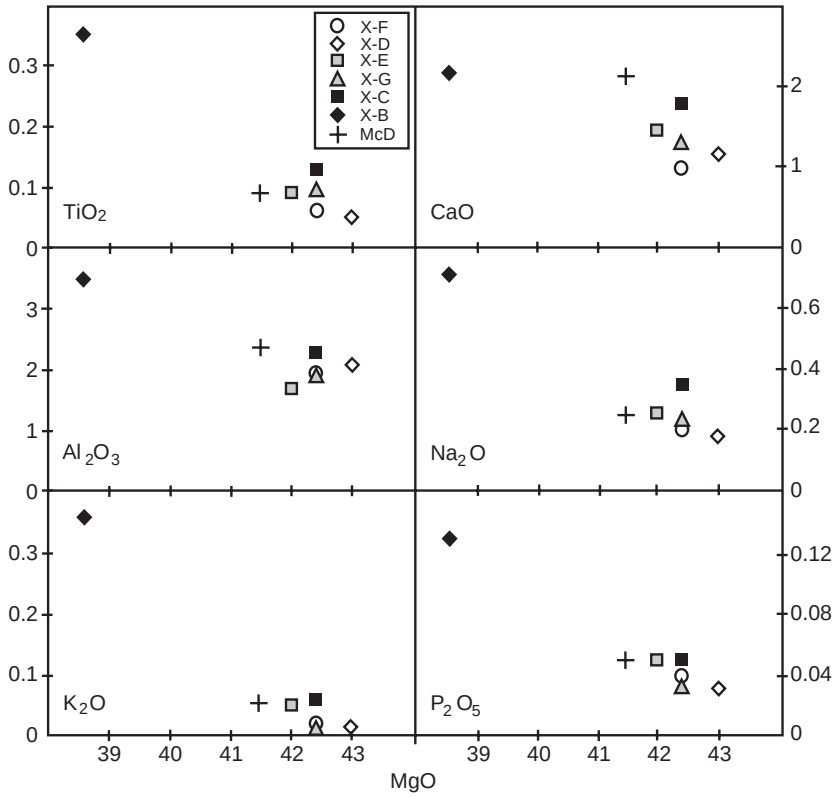

Fig. 4. Whole rock chemistry variation diagram for the Cerro Redondo xenoliths. TiO_2, CaO, Al_2O_3, Na_2O, K_2O, and P_2O_5 (wt.%) are plotted against MgO (wt.%). Sample X-B presents the lowest MgO content (38.6%) and except for CaO, presents considerably higher oxide contents compared with McDonough (1990) reference sample (McD). The other samples form a cluster between 42% and 43% of MgO and do not form clear trends.

6.1. Host basalt

The host basalt (H-B in Table 3) is silica undersaturated and has a K_2O/Na_2O ratio of 0.6. According to the classification of Le Maitre et al. (1989), it belongs to the alkaline series and corresponds to a shoshonitic trachybasalt. The normative nepheline content is 6.7%, confirming the high alkalinity of the basalt. These characteristics correspond to those of the "Post-Plateau" lava sequence defined by Gorring and Kay (2001) for the 7–2 Ma old lavas from Argentine Patagonia. The basalt has highly fractionated REE pattern (La_N/Lu_N=20.5), and a similar trace element composition to ocean island basalt (OIB), a feature commonly observed in "Post-Plateau" basaltic lavas (Gorring and Kay, 2001).

6.2. Xenoliths

Major element compositions of xenoliths are plotted against MgO in Fig. 4. Sample X-B has the lowest MgO content (38.6%), the lowest Mg# (0.89), and the highest contents of TiO_2, CaO, Al_2O_3, Na_2O, K_2O, and P_2O_5, which concentrate into the magma during partial melting, and are here called "basaltic" oxides with values considerably higher than the McDonough average (Table 3). The other five samples form a cluster around 42% and 43% of MgO (Mg#=0.90–0.91) and do not have the clear negative trends (e.g., Al_2O_3) which would be expected in mantle rocks affected by variable extents of melt extraction (McDonough, 1990). Among them, sample X-C shows the highest content of "basaltic" oxides. The modal abundance of clinopyroxene is not correlated with the "basaltic" oxide contents used as a fertility index, indicating that the bulk-rock chemistry is controlled by factors other than the modal phase composition. For example, harzburgite X-F has the lowest modal clinopyroxene content (3%) and also the lowest CaO content, but lherzolites X-D, X-E, X-G, and X-C have similar modal clinopyroxene contents between 10.9% and 11.8% and random "basaltic"

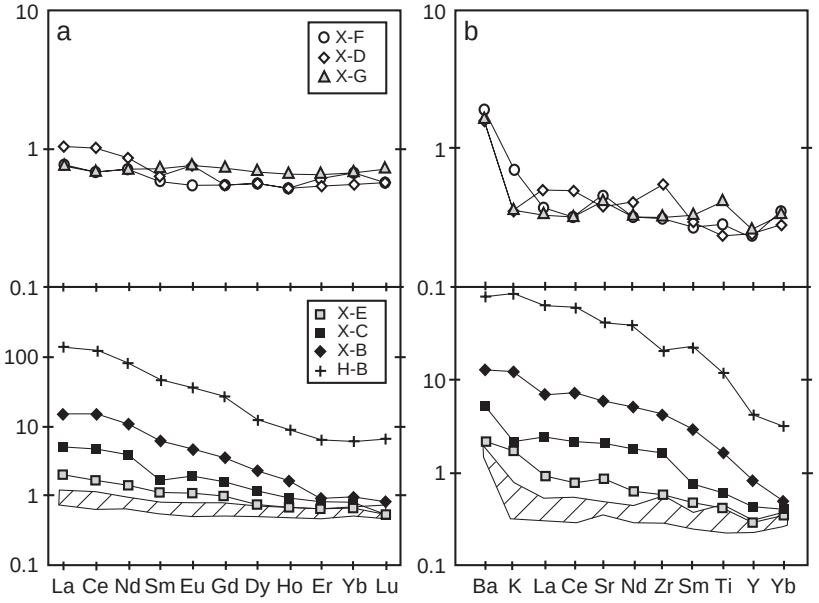

Fig. 5. (a) Chondrite-normalized REE patterns for whole-rock Cerro Redondo xenoliths. Normalization values are from Nakamura (1974), except for Ho taken from Wakita et al. (1971). Flat REE patterns of samples X-F, X-D, and X-G, with concentrations lower than chondrites and progressive increase of LREE for samples X-E, X-C, and X-B. (b) Primitive mantle-normalized trace elements for whole-rock Cerro Redondo xenoliths. Normalization values are from McDonough et al. (1992) except Lu from pyrolite (McDonough and Sun, 1995). Trace element patterns are relatively flat for X-F, X-D, and X-G, with lower concentration than the Primordial Mantle reference, and relatively high content of Ba. There is a progressive increase of incompatible elements contents for samples X-E, X-C, and X-B. Sample X-B concentration mimics that of the host basalt. Shaded areas are fields of samples X-F, X-D, and X-G.

oxide contents. Finally, sample X-B has 8.4% modal clinopyroxene and abnormally high "basaltic" oxide contents.

Fig. 5 shows the trace element variations of the studied xenoliths and the host basalt. Samples X-D, X-F, and X-G are characterized by a relatively flat REE pattern with concentrations generally lower than chondrites (Fig. 5). Sample X-F shows a slightly concave pattern given by a lower concentration of MREE (0.55 for Eu_N and Gd_N) and sample X-D is slightly enriched in LREE compared to the HREE. In the multi-element diagram these three samples show high Ba contents, probably due to weathering, and sample X-D has a small Zr positive anomaly. Samples X-E, X-C, and X-B present a progressive enrichment of LREE and incompatible elements (Fig. 5) with La_N/Lu_N ratios of 2.8, 8.3, and 18.3, respectively. These samples have flat HREE patterns with chondritic concentrations. Trace element concentrations of sample X-B mimic those of the host basalt. None of these patterns correspond to the expected results for melting processes, which would be characterized by variable LREE depletion, and must be explained by some metasomatic process responsible for the variable enrichment of LREE and incompatible elements.

7. Sr–Nd–Pb isotopes

The Sr–Nd–Pb isotopic compositions of whole-rock Cerro Redondo xenoliths and the host lava are presented in Table 4 and plotted in Fig. 6 where the Pali-Aike (Stern et al., 1999; Kempton et al., 1999b) and Gobernador Gregores (Gorring and Kay, 2000; Conceição et al., 2005) xenoliths are also shown. Cerro Redondo xenoliths exhibit a roughly positive trend in the Sr–Nd diagram (Fig. 6a) that is unusual in a common mantle system where normally Nd isotopic ratios decrease with increasing Sr isotopic ratios. This xenolith suite shows $^{87}Sr/^{86}Sr$ ratios ranging from 0.70442 to 0.70519, relatively high values compared to the published data of xenoliths from Patagonia (Fig. 6a), while $^{143}Nd/^{144}Nd$ ratios range from 0.51276 to 0.51297 with values in the lower range of Patagonian xenoliths. Sample X-F has the highest $^{87}Sr/^{86}Sr$ and $^{143}Nd/^{144}Nd$ ratios of 0.70519 and 0.51297, respectively. Sample X-B present the lowest $^{87}Sr/^{86}Sr$ ratio of 0.70442 and an $^{143}Nd/^{144}Nd$ ratio of 0.51279 (only

Table 4
Sr–Nd–Pb isotopic compositions for Cerro Redondo xenoliths and host lava

Sample	Rb (ppm)	Sr (ppm)	$^{87}Rb/^{86}Sr$	$^{87}Sr/^{86}Sr$	SE %	Sm (ppm)	Nd (ppm)	$^{147}Sm/^{144}Nd$	$^{143}Nd/^{144}Nd$	SE %	εNd (t=0)	$^{206}Pb/^{204}Pb$	SE %	$^{207}Pb/^{204}Pb$	SE %	$^{208}Pb/^{204}Pb$	SE %
X-F	0.25	5.05	0.143253	0.705190	0.0020	0.08	0.24	0.194716	0.512972	0.0018	6.5	17.9872	0.0543	15.5555	0.0507	37.9592	0.0543
X-D	0.71	6.93	0.299209	0.705043	0.0020	0.10	1.69	0.036160	0.512823	0.0017	3.6	18.0738	0.8109	15.6058	0.5718	37.3916	0.6766
X-G	0.92	15.67	0.170898	0.704792	0.0010	0.17	0.63	0.158319	0.512838	0.0018	3.9	18.4015	0.0256	15.6058	0.0243	38.2394	0.0244
X-E	0.19	5.01	0.109871	0.705008	0.0013	0.08	0.23	0.216586	0.512759	0.0018	2.4	18.1697	0.0680	15.6084	0.0665	38.2646	0.0374
X-B	6.73	127.77	0.153378	0.704423	0.0020	1.08	5.33	0.122892	0.512786	0.0012	2.9	18.3171	0.0429	15.5979	0.0496	38.5771	0.0426
X-C	2.72	42.56	0.186152	0.704667	0.0024	0.37	0.35	0.643040	0.512906	0.0042	5.2	18.3375	0.1010	15.6509	0.0957	38.5376	0.1048
H-B	46.50	946.26	0.143004	0.704474	0.0017	9.34	47.26	0.119501	0.512790	0.0022	2.3	18.4243	0.1769	15.6479	0.1883	38.7279	0.1863

SE%: standard error percent; εNd (t=0): Epsilon neodymium notation.

sample X-E has slightly lower $^{143}Nd/^{144}Nd$ ratio of 0.51276), with values notably similar than those obtained for the host basalt (0.70447 and 0.51279, respectively). In the $^{87}Sr/^{86}Sr$ versus $^{143}Nd/^{144}Nd$ covariation diagram (Fig. 6a) these samples plot to the right side of the Patagonia plateau basalt field given by Stern et al. (1990) and only sample X-B falls in this field.

Samples X-F and X-D yield the least radiogenic Pb while the other samples plot toward the Pb isotopic contents of the host basalt (Fig. 6b, c). The $^{206}Pb/^{204}Pb$ ratio in these samples is 17.987 and 18.074, respectively, while in the other samples this ratio ranges from 18.170 to 18.402. The $^{207}Pb/^{204}Pb$ ratio for samples X-F and X-D is 15.556 and 15.606, respectively, and ranges from 15.598 to 15.651 in the other samples. The $^{208}Pb/^{204}Pb$ ratio in samples X-F and X-D is 37.392 and 37.959, respectively, in samples X-G and X-E is 38.239 and 38.265, respectively, and is considerably higher in samples X-C and X-B with values of 38.538 and 38.577, respectively.

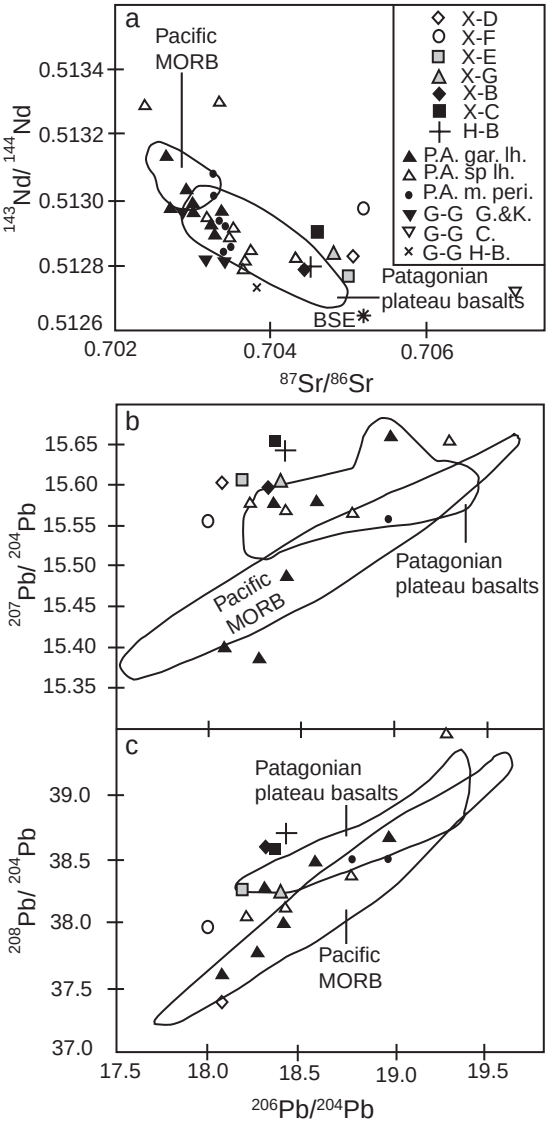

Fig. 6. $^{87}Sr/^{86}Sr$ vs. $^{143}Nd/^{144}Nd$ plot, and $^{206}Pb/^{204}Pb$ vs. $^{207}Pb/^{204}Pb$ and vs. $^{208}Pb/^{204}Pb$ plots for xenoliths from Cerro Redondo. Also shown are published data of Pali-Aike garnet and spinel lherzolites (*P.A. gar. lh* and *P.A. sp. lh*, respectively) and Pali-Aike metasomatized peridotites (*P.A. m. peri*) (Stern et al., 1999; Kempton et al., 1999a,b), Gobernador Gregores xenoliths (*G-G G. and K.*; Gorring and Kay, 2000, and *G-G C.*; Conceição et al., 2005), and the host basalts from Cerro Redondo and Gobernador Gregores xenoliths (*H-B* and *G-G H-B.*, respectively). (a) High $^{87}Sr/^{86}Sr$ ratios in Cerro Redondo xenoliths and similar $^{143}Nd/^{144}Nd$ ratios compared to other xenoliths from Patagonia, producing an abnormal positive trend for mantle derived rocks. Sample X-B has almost identical Sr–Nd isotopic ratios to the host basalt. (b–c) Samples X-F and X-D have the lowest radiogenic Pb of all Cerro Redondo xenoliths, plotting away from the Patagonian plateau basalts field. Samples X-C and X-B have in general the highest radiogenic Pb, with values close to those obtained for the host basalt.

8. Discussion

8.1. The relationships between textural, geochemical, and isotopic characteristics

The petrographic, geochemical, and isotopic characteristics of the six studied xenoliths from Cerro Redondo present gradational variations. The increase of disequilibrium textures is coincident with the increase of TiO_2, CaO, Al_2O_3, Na_2O, K_2O, P_2O_5, LREE, and other incompatible elements concentrations (Figs. 2, 4 and 5). These characteristics are thought to be a consequence of increasing modification of the xenoliths by host basalt infiltration and reaction, producing progressive variation of the radiogenic Sr, Nd, and Pb contents towards the host basalt composition, the most modified xenoliths plotting closer to the host basalt (Fig. 6). This modification process would be responsible for the unusual positive

trend observed in the $^{87}Sr/^{86}Sr$ versus $^{143}Nd/^{144}Nd$ diagram (Fig. 6) as for the heating event recorded by mineral rim compositions. According with this hypothesis, samples X-F and X-D suffered no, or very little host basalt infiltration since they conserve equilibrium textures in their mineral assemblage, and have the lowest TiO_2, CaO, Na_2O, K_2O, and P_2O_5 contents, flat chondrite normalized REE pattern, the most radiogenic Sr and Nd (X-F), and the least radiogenic Pb. Samples X-G and X-E have incipient host basalt contamination, and samples X-C and X-B are the most modified xenoliths, with abundant disequilibrium textures, significant enrichments of TiO_2, CaO, Al_2O_3, Na_2O, K_2O, and P_2O_5, LREE

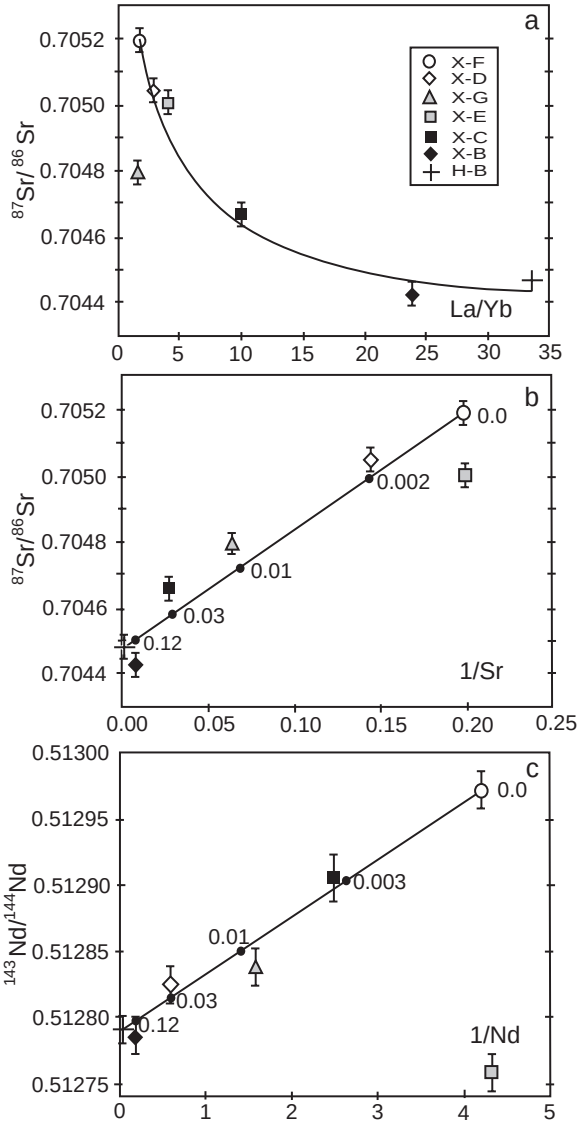

Fig. 7. (a) Plot of $^{87}Sr/^{86}Sr$ vs. La_N/Yb_N ratios of Cerro Redondo xenoliths and host basalt showing a roughly hyperbolic trend thought to represent mixing between xenoliths and host basalt. (b–c) Plots of 1/Sr and 1/Nd versus $^{87}Sr/^{86}Sr$ and $^{143}Nd/^{144}Nd$, respectively, for Cerro Redondo xenoliths and host basalt, showing a linear variation expected in a mixing process. The numbers on the curves were estimated by a simple mixing model and express the weight fraction of the basalt in the mixture. The values obtained from these two models differs considerably, probably has a consequence of the different behavior of these elements in the mixing processes.

and incompatible elements, especially in X-B. This sample is strongly isotopically homogenized with the host basalt, with almost identical Sr and Nd ratios.

8.2. Contamination estimates by a simple model

The hyperbolic trend observed in the graph of $^{87}Sr/^{86}Sr$ versus La_N/Yb_N (Fig. 7a) is interpreted as a consequence of mixing between xenoliths and host basalt. In Fig. 7b and c, values of 1/Sr and 1/Nd (Sr and Nd from Table 4), are plotted versus $^{87}Sr/^{86}Sr$ and $^{143}Nd/^{144}Nd$ ratios, respectively, and reasonably straight mixing lines are obtained. The end members in both diagrams are sample X-F and host basalt, and the most contaminated xenoliths is X-B. Different degrees of contamination were obtained for samples X-D and X-C, probably reflecting the different behavior of Sr and Nd during the basalt infiltration process. Contamination values from the Sr system are more concordant with the petrographic, major, and trace element variation (Section 8.1) than those for the Nd system, so we believe these values are better representative of the mixing process. They are 0.002, 0.01, 0.03, and 0.12 weight fractions on samples X-D, X-G, X-C, and X-B, respectively (Fig. 7b). Sample X-E falls off both mixing lines, suggesting that this sample either suffered different isotopic modifications during the interaction with the host basalt, or it comes from a different source (see discussion below).

To check this simple model we used the mass balance equation:

$$C_i = \text{X-F}_i \times (1 - f) + f \times \text{H-B}_i \quad (1)$$

where X-F_i is the concentration of element i in sample X-F, H-B_i is the concentration of the element i in host basalt (H-B), f is the weight fraction of the infiltrated host basalt, and C_i is the concentration of element i in the mixture of xenolith X-F and host basalt. This very simple model assumes that the host basalt infiltrates each xenolith either without interaction or with closed system interaction after infiltration. We calculate C for the four values of f obtained from the simple mixing model of Fig. 7b (0.002 (X-D), 0.01(X-G), 0.03 (X-C), and 0.12 (X-B)) that were labeled C1, C2, C3, and C4, respectively. In Table 5 we compare the calculated compositions of some major and REE, with those obtained from the whole rock analyzes,

Table 5
Comparison of some major and REE, between samples X-D, X-G, X-C, and X-B and modeled C1, C2, C3, and C4 compositions, calculated using contamination factors of 0.002, 0.01, 0.03, and 0.12 weight fractions, respectively, in Eq. (1)

Sample	X-F	H-B	C1	X-D	C1-X-D	%	C2	X-G	C2-X-G	%	C3	X-C	C3-X-C	%	C4	X-B	C4-X-B	%
			(f=0.002)				(f=0.01)				f=0.03				f=0.12			
TiO_2	0.06	2.55	0.06	0.05	0.01	20	0.08	0.09	−0.01	11	0.13	0.13	0.00	0	0.36	0.35	0.01	3
Al_2O_3	1.94	14.71	1.97	2.07	−0.09	5	2.07	1.90	0.17	9	2.32	2.26	0.06	3	3.47	3.47	0.00	0
MgO	42.39	7.56	42.32	43.00	−0.68	2	42.04	42.40	−0.36	1	41.35	42.40	−1.05	2	38.21	38.60	−0.39	1
CaO	0.97	6.06	0.98	1.16	−0.18	16	1.02	1.28	−0.26	20	1.12	1.78	−0.66	37	1.58	2.16	−0.58	27
Na_2O	0.20	4.30	0.21	0.18	0.03	16	0.24	0.23	0.01	4	0.32	0.35	−0.03	9	0.69	0.71	−0.02	3
K_2O	0.02	2.60	0.03	0.01	0.02	200	0.05	0.01	0.04	400	0.10	0.06	0.04	67	0.33	0.36	−0.03	8
P_2O_5	0.04	0.82	0.04	0.03	0.01	33	0.05	0.03	0.02	67	0.06	0.05	0.01	20	0.13	0.13	0.00	0
Trace element																		
La	0.26	46.00	0.35	0.35	0.00	0	0.72	0.25	0.47	188	1.63	1.70	−0.07	4	5.75	5.00	0.75	15
Ce	0.60	108.00	0.81	0.90	−0.09	10	1.67	0.60	1.07	178	3.82	3.90	−0.08	2	13.49	13.10	0.39	3
Nd	0.45	54.00	0.56	0.55	0.01	2	0.99	0.46	0.53	115	2.06	2.40	−0.34	14	6.88	6.95	−0.07	1
Sm	0.12	9.87	0.14	0.13	0.01	8	0.22	0.15	0.07	47	0.41	0.33	0.08	24	1.29	1.28	0.01	1
Eu	0.04	2.75	0.05	0.06	−0.01	17	0.07	0.06	0.01	17	0.12	0.15	−0.03	20	0.37	0.36	0.01	3
Gd	0.15	7.28	0.16	0.15	0.01	7	0.22	0.20	0.02	10	0.36	0.43	−0.07	16	1.01	1.00	0.01	1
Dy	0.20	4.27	0.21	0.19	0.02	11	0.24	0.24	0.00	0	0.32	0.39	−0.07	18	0.69	0.78	−0.09	12
Ho	0.04	0.70	0.04	0.04	0.00	0	0.05	0.05	0.00	0	0.06	0.07	−0.01	14	0.12	0.13	−0.01	8
Er	0.14	1.43	0.14	0.12	0.02	17	0.15	0.15	0.00	0	0.18	0.18	0.00	0	0.29	0.21	0.08	38
Yb	0.15	1.38	0.15	0.12	0.03	25	0.16	0.15	0.01	6	0.19	0.17	0.02	12	0.30	0.21	0.09	43
Lu	0.02	0.23	0.02	0.02	0.00	0	0.02	0.03	−0.01	33	0.03	0.02	0.01	50	0.05	0.03	0.02	67

Considerably good approximation for C1, C3, and C4 with analyzes of samples X-D, X-C, and X-B, respectively. Significant differences between sample X-G and C2 especially in LREE and between HREE contents of C4 and X-B.

and in Fig. 8 we show the comparison for the REE. The calculated concentrations for C1, C3 and C4 are reasonably good approximation of the analyzed concentrations of samples X-D, X-C, and X-B, respectively (Table 5; Fig. 8), showing that the estimated contamination factors are correct. Significant differences exist between HREE contents of C4 and X-B, suggesting a selective enrichment of xenoliths in the most incompatible elements during the interaction with the infiltrating basalt. The low MgO content of sample X-B could also be explained by this mixing process. On the other hand, C2 has considerably higher LREE contents than sample X-G (Table 5), showing that the 0.01 contamination factor determined by the Sr and Nd systems is not reflected by the major and trace element geochemistry. The opposite case is represented by sample X-E with similar REE pattern to C2 (Figs. 5 and 8), suggesting 1% of basalt infiltration, but which is not reflected by Sr and Nd isotopes. Both samples present incipient disequilibrium textures ascribed to the host basalt interaction influence and similar petrographic and whole rock major chemistry. We propose that samples X-G and X-E came from the same mantle source as the other studied xenoliths, but suffered selective isotopic and trace element modifications, respectively; the reason for which is unclear.

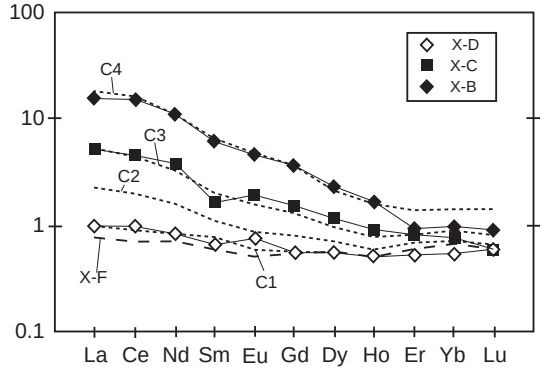

Fig. 8. Correlation between measured REE contents of samples X-D, X-C, and X-B, and the modeled compositions C1, C3, and C4 (dotted lines), calculated for 0.2%, 3%, and 12% of host basalt contamination, respectively. Calculated HREE contents of C4 are significantly higher than in the analyzed sample X-B. Sample X-G is not shown but its flat REE pattern (Fig. 5) contrasts considerably with the slightly steep pattern of C2, calculated with a 1% of contamination. Sample X-F is represented as dashed line.

However, some authors (Bodinier et al., 1990; Pedersen et al., 1996; Vernières et al., 1997; Shaw, 1999 between others) have shown that complex reactions between basalt veins and xenoliths produce gradual changes in phase assemblages and their mineral compositions. In addition, the basaltic melts evolve to form silicic melts as the result of reaction between infiltrating basaltic melt and peridotite wall-rock. The brownish veins of Cerro Redondo xenoliths, in some cases related to the basalt infiltration (Fig. 2h), have variable compositions which differ from the host basalt and any of the mineral phases (Table 2). In sample X-B, for example, a CaO rich vein related to the host basalt infiltration was analyzed. These variations are probably related to the complex relation of dissolution and precipitation between wall rock xenoliths and the iniltrating basalt, showing once again the weakness of the simple model.

8.3. Implications of the petrogenetic model

The model proposed above, implies that the studied xenoliths come from the same source, with similar petrographic, geochemical, and isotopic characteristics. *P–T* estimates (Fig. 3) indicate a wide range of provenance for the xenolith suite, between 12 and 21 kb (36 to 63 km depth) suggesting that the deep mantle column sampled by Cerro Redondo xenoliths is quite homogeneous.

The collection of the xenoliths by the magma probably began at the spinel-garnet transition (Fig. 3), continued at least until 12 km depth, and was caused by the rupture of peridotitic wall-rock by the ascending magma possibly through hydraulic fracturing. The magma and the included xenoliths probably accumulated at very shallow depth in the sill-like magma reservoir identified in the Cerro Redondo structure. Different times of residence in the basalt and different sizes of the hosted xenoliths could be responsible for different degrees of basalt infiltration. Klügel (1998) determined periods from days to decades of residence for xenoliths from La Palma based on a model of interdiffusion of Fe–Mg, so similar periods of time could be responsible for the modifications of Cerro Redondo xenoliths.

The unmodified xenolith X-F best represents the characteristics of the lithospheric mantle column having the highest Sr and Nd isotope ratios, and

showing a decoupling of the Nd–Sr system in which increasing in $^{87}Sr/^{86}Sr$ ratios, with values higher than most other Patagonian xenoliths except for one sample from Lote 17 (Conceição et al., 2005) are not accompanied by an increase in $^{143}Nd/^{144}Nd$ ratios. This is in disagreement with the hypothesis that the xenoliths came from a lithospheric mantle depleted in a previous basalt extraction process, and must be explained by some other process such as chromatography (Navon and Stolper, 1987) in the mantle.

9. Conclusions

The six mantle xenoliths studied here present different stages of interaction with the host basalt producing a gradational variation in their petrographic, geochemical, and isotopic characteristics. This variation consists on a progressive increment of disequilibrium textures, and progressive enrichment of the "basaltic" oxides TiO_2, CaO, Al_2O_3, Na_2O, K_2O, P_2O_5, light rare earth elements (LREE), and other incompatible elements, with increasing infiltration of the host basalt. The Sr, Nd, and Pb isotopic compositions vary between those of the unmodified sample X-F and those of the host basalt isotopic compositions. A simple mixing model based on Sr isotopes, largely corroborated by mass balance of major and trace elements, yielded coherent contamination values of 0.2%, 3%, and 12% for samples X-D, X-C and X-B, respectively. Samples X-G and X-E apparently suffered a ~1% selective modification of the isotopic and trace chemistry, respectively, but the cause is unknown. Modifications started during magma transport and continued during the residence in the sill-like, subvolcanic magma chamber interpreted for the Cerro Redondo edifice.

Sample X-F, the end member in our mixing model, represents the unmodified mantle. It suffered some previous enrichment in radiogenic Sr, without disturbance of their Nd system. Core compositions of minerals indicate a *P–T* range of 12.4 kb to 21.4 kb (Mercier et al., 1984) and of 823 °C to 1043 °C (Brey and Köhler, 1990), respectively constraining a geothermal gradient similar to a previous reported geothermal gradient for lithospheric mantle under Pali-Aike in Southern Patagonia of 65 mW/m^2 (Stern et al., 1999).

Acknowledgements

Science Research Project no. 13373004 (to R. Anma) from the Ministry of Education, Culture, Sport, Science and Technology, Japan, supported sampling of Cerro Redondo. Dr. Y. Orihashi supplied the samples utilised in this study. We thank Mr. D. Hirata for his guidance during fieldwork, C.A. Cingolani for our introduction to the "mantle realm", R. Pankhurst for language corrections and comments, and F. Chemale Jr. for analytical help. Thanks are also due to D. Demaiffe for discussions in early stages of this work, B. Deruelle for the microprobe analyses performed in Université Pierre et Marie Cuire, Paris 6, France. Constructive reviews by G. Rivalenti, R. Fodor and I. McReath are greatly appreciated. A CONICYT doctoral fellowship to MS, PROSUL-CNPq (Project AC-74) and project EU-CONICYT C1ICT930033 funded this work.

References

Bertrand, P., Mercier, J.-C.C., 1985. The mutual solubility of coexisting ortho- and clinopyroxene: toward an absolute geothermometer for natural system? Earth Planet. Sci. Lett. 6 (1–2), 109–122.

Bodinier, J.L., Vasseur, G., Vernieres, J., Dupuy, C., Fabriès, J., 1990. Mechanisms of mantle metasomatism: geochemical evidence from the Lherz orogenic peridotite. J. Petrol. 31, 597–628.

Brey, G.P., Köhler, T., 1990. Geothermobarometry in four-phase lherzolites: II. New thermobarometers, and practical assessment of existing thermobarometers. J. Petrol. 31, 1353–1378.

Cande, S.M., Leslie, R.B., 1986. Late Cenozoic tectonics of the southern Chile Trench. J. Geophys. Res. 91, 471–497.

Chapman, D.S., 1986. Thermal gradients in the continental crust. In: Dawson, J.B., Carswell, D.A., Hall, J., Wedepohl, K.H. (Eds.), The Nature of the Lower Continental Crust, vol. 24. Spec. Publ.-Geol. Soc. Lond., pp. 63–70.

Ciuffi, S., Rivalenti, G., Vannucci, R., Zanetti, A., Mazzucchelli, M., Cingolani, C.A., 2002. Geochemical variations in the host basalts-derived glasses infiltrating mantle xenoliths. CD-ROM XV Congreso Geológico Argentino, El Calafate.

Conceição, R.V., Mallmann, G., Koester, E., Schilling, M., Bertotto, G.W., Rodriguez-Vargas, A., 2005. Andean subduction-related mantle xenoliths: isotopic evidence of Sr-Nd decoupling during metasomatism. Lithos 82, 273–287, this issue.

Gorring, M.L., Kay, S.M., 2000. Carbonatite metasomatized peridotite xenoliths from southern Patagonia: implications for lithospheric processes and Neogene Plateau magmatism. Contrib. Mineral. Petrol. 140, 55–72.

Gorring, M.L., Kay, S.M., 2001. Mantle processes and sources of Neogene slab window magmas from southern Patagonia, Argentina. J. Petrol. 42 (6), 1067–1094.

Gorring, M.L., Kay, S.M., Zeitler, P.K., Ramos, V.A., Panza, J.L., Rubiolo, D., Fernandez, M.I., 1997. Neogene patagonian plateau lavas: continental magmas associated with ridge collision at the Chile triple junction. Tectonics 16, 1–17.

Kempton, P.D., Lopez-Escobar, L., Hawkesworth, C.J., Pearson, G., Ware, A.J., 1999a. Spinel±garnet lherzolite xenoliths from Pali Aike: Part 1. Petrography, mineral chemistry and geothermobarometry. In: Gurney, J.J., Gurney, J.L., Pascoe, M.D., Richardson, S.H. (Eds.), Proc. 7th International Kimberlite Conference, The J.B. Dawson Volume. Red Rood Design, Cape Town, pp. 403–414.

Kempton, P.D., Hawkesworth, C.J., Lopez-Escobar, L., Ware, A.J., 1999b. Spinel±garnet lherzolite xenoliths from Pali Aike: Part 2. Trace element and isotopic evidence bearing on the evolution of lithospheric mantle beneath southern Patagonia. In: Gurney, J.J., Gurney, J.L., Pascoe, M.D., Richardson, S.H. (Eds.), Proc. 7th International Kimberlite Conference, The J.B. Dawson Volume. Red Rood Design, Cape Town, pp. 415–428.

Kilian, R., Stern, C.R., 2002. Constraints on the interaction between slab melts and the mantle wedge from adakitic glass in peridotite xenoliths. Eur. J. Mineral. 14 (1), 25–36.

Klügel, A., 1998. Reactions between mantle xenoliths and host magma beneath La Palma (Canary Island): constraints on magma ascent rates and crustal reservoirs. Contrib. Mineral. Petrol. 131, 237–257.

Köhler, T.P., Brey, G.P., 1990. Calcium exchange between olivine and clinopyroxene calibrated as a geothermobarometer for natural peridotites from 2 to 60 kb with applications. Geochim. Cosmochim. Acta 54, 2375–2388.

Laurora, A., Mazzucchelli, M., Rivalenti, G., Vannucci, R., Zanetti, A., Barbieri, M.A., Cingolani, C.A., 2001. Metasomatism and melting in carbonated peridotite xenoliths from the mantle wedge: the Gobernador Gregores case (southern Patagonia). J. Petrol. 42 (1), 69–87.

Le Maitre, R.W., Bateman, P., Dudek, A., Keller, J., Lameyre Le Bas, M.J., Sabine, P.A., Schmid, R., Sorensen, H., Streckeisen, A., Woolley, A.R., Zanetti, B., 1989. A Classification of Igneous Rocks and Glossary of Terms. Blackwell, Oxford.

McDonough, W.F., 1990. Constraints of the composition of the continental lithospheric mantle. Earth Planet. Sci. Lett. 101, 1–18.

McDonough, W.F., Sun, S., 1995. The composition of the Earth. Chem. Geol. 120 (3–4), 223–253.

McDonough, W.F., Sun, S., Ringwood, A.E., Jagoutz, E., Hofmann, A.W., 1992. Potassium, rubidium and cesium in the Earth and Moon and the evolution of the mantle of the earth. Geochim. Cosmochim. Acta 56, 1001–1012.

Mercier, J.-C.C., Nicolas, A., 1975. Textures and fabrics of upper mantle peridotites as illustrated by basalt xenoliths. J. Petrol. 16 (2), 454–487.

Mercier, J.-C.C., Benoit, V., Girardeau, J., 1984. Equilibrium state of diopside-bearing harzburgites from ophiolites: geobarometric and geodynamic implications. Contrib. Mineral. Petrol. 85, 391–403.

Nakamura, N., 1974. Determination of REE, Ba, Fe, Mg, Na and K in carbonaceus and ordinary chondrites. Geochim. Cosmochim. Acta 38, 755–757.

Navon, O., Stolper, E., 1987. Geochemical consequences of melt percolation: the upper mantle as a chromatographic column. J. Geol. 95, 285–307.

O'Neill, H.St.C., 1981. The transition between spinel lherzolite and garnet lherzolite and its use as a geobarometer. Contrib. Mineral. Petrol. 77, 185–194.

Pedersen, W., Neumann, E.-R., Jensen, B., 1996. The upper mantle under La Palma, Canary Island: formation of Si–K–Na-rich melt and its importance as a metasomatic agent. Contrtib. Mineral. Petrol. 125, 113–139.

Ramos, V.A., Niemeyer, H., Skarmeta, J., Muñoz, J., 1982. Magmatic evolution of the austral Patagonian andes. Earth Sci. Rev. 18, 411–443.

Schilling, M., 2002. Estudio petrográfico y geoquímico de enclaves ultramáficos contenidos en basalto alcalino de Cerro Redondo de edad Pliocena-Pleistocena, provincia de Santa Cruz, Patagonia Argentina. Graduation thesis, Departamento de Geología, Universidad de Chile, 86 p.

Shaw, C.S.J., 1999. Dissolution of orthopyroxene in basaltic magma between 0.4 and 2 GPa: further implications for the origin of Si-rich alkaline glass inclusions in mantle xenoliths. Contrib. Mineral. Petrol. 135, 114–132.

Soto, J.I., Soto, V.M., 1995. PTMAFIC: software package for thermometry, barometry, and activity calculations in mafic rocks using an IBM-compatible computer. Comput. Geosci. 21 (5), 619–652.

Stern, C.R., Futa, K., Zartman, R.E., Peng, Z., Kyser, T.K., 1990. Trace-element and Sr, Nb, Pb, and O isotopic composition of Pliocene and Quaternary alkali basalts of the Patagonian Plateau lavas of southernmost South America. Contrib. Mineral. Petrol. 104, 294–308.

Stern, C.R., Kilian, R., Olker, B., Hauri, E.H., Kyser, T.K., 1999. Evidence from mantle xenoliths for relatively thin (<100 km) continental lithosphere below the Phanerozoic crust of southernmost South America. Lithos 48, 217–235.

Vernières, J., Godard, M., Bodinier, J.L., 1997. A plate model for the simulation of trace element fractionation during partial melting and magma transport in the Earth's upper mantle. J. Geophys. Res. 102 (B11), 24.771–24.784.

Wakita, H., Rey, P., Schmitt, R.A., 1971. Abundances of the 14 rare-earth elements and 12 other trace elements in Apolo II samples: five igneous and one breccia rocks and four soils. Proc. 2nd Lunar Sci. Conf.. Pergamon Press, Oxford, pp. 1319–1329.

Wood, B.J., Banno, S., 1973. Garnet–orthopyroxene and orthopyroxene–clinopyroxene relationships in simple and complex systems. Contrib. Mineral. Petrol. 42, 109–124.